Key Points:
- Mode converted UH waves decay to electron Bernstein waves
- Electron Bernstein waves exceed threshold of stochasticity to become primary source of bulk heating
- Average temperature exceeds threshold for fast acceleration by Langmuir waves

Correspondence to:
A. Najmi,
Chris.Najmi@jhuapl.edu

Simulations of ionospheric turbulence produced by HF heating near the upper hybrid layer

A. Najmi[1,2], B. Eliasson[3], X. Shao[2], G. M. Milikh[2], and K. Papadopoulos[2]

[1]The Johns Hopkins University Applied Physics Laboratory, Laurel, Maryland, USA, [2]Departments of Physics and Astronomy, University of Maryland, College Park, Maryland, USA, [3]SUPA, Department of Physics, University of Strathclyde, UK

Abstract Heating of the ionosphere by high-frequency (HF), ordinary (*O*) mode electromagnetic waves can excite magnetic field-aligned density striations, associated with upper and lower hybrid turbulence and electron heating. We have used Vlasov simulations in one spatial and two velocity dimensions to study the induced turbulence in the presence of striations when the *O*-mode pump is mode converted to large-amplitude upper hybrid oscillations trapped in a striation. Parametric processes give rise to upper and lower hybrid turbulence, as well as to large amplitude, short wavelength electron Bernstein waves. The latter excite stochastic electron heating when their amplitudes exceed a threshold for stochasticity, leading to a rapid increase of the electron temperature by several thousands of kelvin. The results have relevance for high-latitude heating experiments.

1. Introduction

Magnetic field-aligned striations (FAS) are plasma density depletions which are frequently produced by electrostatic processes during high-frequency (HF) ordinary (*O*) mode heating of the ionosphere. Small-scale FAS have transverse sizes of a few meters [*Rao and Thome*, 1974; *Franz et al.*, 1999], while their sizes along the magnetic field are several tens of kilometers [*Dysthe et al.*, 1982; *Gurevich et al.*, 1995]. Striations typically form on timescales of the order of seconds after the heating beam is switched on, and similarly, they dissipate on the order of seconds after the heating is switched off. Once formed, an incident electromagnetic wave is mode converted to upper hybrid waves trapped in the striation, heating the electrons, and further increasing the density depletion. The mode conversion leads to anomalous absorption of the *O*-mode wave near the altitude of the ionospheric upper hybrid resonance [*Gurevich*, 2007].

Following the upgrade of the High-Frequency Active Auroral Research Program (HAARP) heater to effective radiated powers (ERPs) up to 5 GW, *Pedersen et al.* [2009] observed descending artificial ionospheric layers (DAILs). The DAILs are believed to be formed due to the ionization of the neutral gas by suprathermal electrons accelerated by the induced ionospheric turbulence [*Mishin and Pedersen*, 2011]. Once the layer reaches sufficient density to reflect the pump wave, the interaction region shifts downwards, creating the DAILs. *Eliasson et al.* [2012] employed a multiscale numerical model of the generation and descent of DAILs and found that the bulk electron temperature needs to exceed 4000 K for a significant fraction of the electrons in the tail of the distribution function to be efficiently accelerated by the turbulence. A possible scenario is that the bulk electrons are first heated at the upper hybrid layer, and as the hot electrons reach the critical layer, they are further accelerated by strong Langmuir turbulence to form high-energy tails.

The commonly discussed mechanism of electron heating near the upper hybrid layer involves collisional Ohmic heating by mode converted upper hybrid waves trapped in FAS [*Dysthe et al.*, 1982; *Gurevich et al.*, 1995]. In the weakly collisional plasma of the *F* region ionosphere, the Ohmic heating of electrons takes place on timescales of the order of seconds. However, a potentially faster and more efficient mechanism is stochastic heating, which takes place in the presence of large-amplitude electric field gradients [*Fukuyama et al.*, 1977; *Karney*, 1978; *McChesney et al.*, 1987; *Balikhin et al.*, 1993; *Stasiewicz et al.*, 2000]. As the amplitude exceeds a threshold for stochasticity, the particle orbits become unstable and diverge in time, leading to a very rapid heating of the plasma. Stochastic heating is favored by small-scale turbulence involving large amplitude, short wavelength electrostatic waves.

The aim of this paper is to investigate stochastic electron heating near the upper hybrid layer, by means of Vlasov simulations relevant to ionospheric heating experiments. The paper is organized as follows: In section 2, we describe the simulation model and numerical parameters. We present an overview of the simulation results, specifically addressing density fluctuations, electron heating, and upper and lower hybrid wave modes in section 3. In section 4 we discuss a theory of the observed parametric decay processes, and the electron heating by short wavelength electron Bernstein waves is studied in section 5. Finally, we give a summary and conclusions in section 6.

2. Numerical Model and Simulation Setup

To study the collisionless heating of electrons in small-scale FAS, we have carried out electrostatic Vlasov simulations in one spatial and two velocity dimensions. To eliminate the effects of numerical noise in the simulations, we solve the Vlasov equation in position and velocity space using a Fourier method in velocity space [*Eliasson*, 2010]. The simulation domain is along the x axis while the velocity is in the (v_x, v_y) space. The Vlasov equation describes the evolution of the distribution function f_α of charged particles of species α (where α equals i and e for ions and electrons, respectively) in position and velocity space,

$$\frac{\partial f_\alpha}{\partial t} + v_x \frac{\partial f_\alpha}{\partial x} + \frac{\vec{F}_\alpha}{m_\alpha} \cdot \nabla_v f_\alpha = 0, \tag{1}$$

where

$$\vec{F}_\alpha = q_\alpha \left(\vec{E} + \vec{E}_{ext} + \vec{v} \times \vec{B}_0 \right) \tag{2}$$

is the Lorentz force, q_α and m_α are the particle's charge and mass, $q_e = -e$ and $q_i = e$, and e is the magnitude of the electron charge. The constant magnetic field $\vec{B}_0 = \hat{z}B_0$ is directed along the z axis. The O-mode pump wave is represented by an external oscillating dipole electric field $\vec{E}_{ext} = \hat{x}E_0 \sin(\omega_0 t)$ directed along the x axis at frequency $\omega_0 = 21.59 \times 10^6 \text{s}^{-1}$ and with amplitude E_0. The frequency ω_0 corresponds to the F_2 peak during night time heating experiments. We are using the electrostatic approximation $\vec{E} = -\hat{x}\partial\phi/\partial x$ for the electric field, where the electrostatic potential is obtained from the Poisson equation

$$-\frac{\partial^2 \phi}{\partial x^2} = \frac{\rho}{\epsilon_0}. \tag{3}$$

Here the electron charge density is

$$\rho = \sum_{\alpha=i,e} q_\alpha n_\alpha, \tag{4}$$

and the particle number density

$$n_\alpha(\vec{x}, t) = \int \int f_\alpha(\vec{x}, \vec{v}, t) dv_x dv_y. \tag{5}$$

The size of the one-dimensional spatial simulation domain of 9 m resolved by 600 points, giving a grid spacing of 1.5 cm, and the simulation time is about 300 µs over a total of 84,000 time steps that are dynamically chosen during the simulation to maintain numerical stability resulting in an average time step of about 4 ns. The initial electron and ion temperatures are set to $T_{e0} = 1500$ K and $T_{i0} = 1000$ K, consistent with measurements of ionospheric temperatures before heating using incoherent scatter radars [*Blagoveshchenskaya et al.*, 2011a, 2011b], using Maxwellian electron and ion velocity distributions. In velocity space, we chose a two-dimensional grid of 160×160 points for both the electrons and ions. For the electrons, the velocity space covers the range $\pm 25 v_{Te0}$ in the v_x and v_y directions, while for the ions it covers the range $\pm 17.6 v_{Ti0}$ where $v_{Te0} = \sqrt{k_B T_{e0}/m_e} = 1.508 \times 10^5$ m/s is the electron thermal speed and $v_{Ti0} = \sqrt{k_B T_{i0}/m_i} = 2.873 \times 10^3$ m/s is the ion thermal speed.

As initial conditions for the electron and ion number densities, we use an ambient density of $n_0 = 1.27 \times 10^{11}$ m^{-3}, with a Gaussian density striation superimposed on the background density,

$$n_i(x) = n_e(x) = n_0 \left[1 - \alpha \exp\left(-x^2/R^2\right) \right], \tag{6}$$
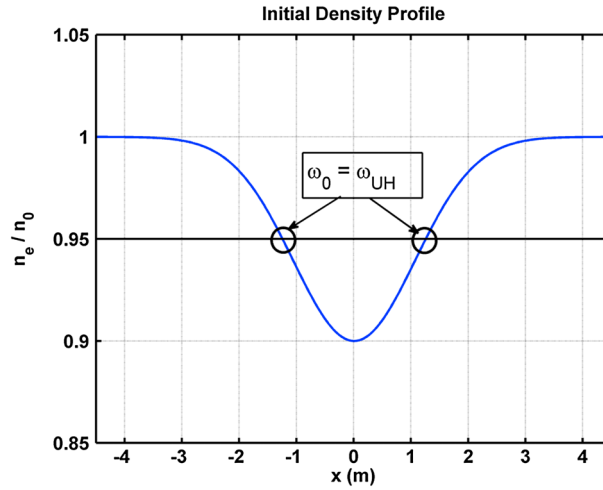
Initial Density Profile

Figure 1. Simulation overview: The profile of the initial density striation with the density at $\omega_0 = \omega_{UH}$ indicated.

with a relative density depletion of $\alpha = 0.1$ and transverse size of $R = 1.5$ m. A schematic of the simulation setup is shown in Figure 1. The ambient electron density $n_e = n_0$ corresponds to $\omega_{pe} = 20.09 \times 10^6 s^{-1}$ far away from the striation. An external magnetic field $B_0 = 5.17 \times 10^{-5}$ T, the approximate magnetic field is applied, corresponding to $\omega_{ce} = 9.09 \times 10^6 s^{-1}$. The pump wave frequency ω_0 is chosen such that it equals the local upper hybrid frequency $\omega_{UH}(x) = \sqrt{\omega_{pe}^2(x) + \omega_{ce}^2}$ at the edges of the striation where $n_e = 0.95n_0$, where $\omega_{pe}(x) = \sqrt{n_e(x)e^2 / (\epsilon_0 m_e)}$ is the local electron plasma frequency and $\omega_{ce} = eB_0/m_e$ is the electron cyclotron frequency giving $\omega_0 = 21.59 \times 10^6 s^{-1}$ (3.436 MHz).

The most common ion species at the F_2 layer is atomic oxygen, but for numerical efficiency, we use the proton-to-electron mass ratio $m_i/m_e = 1836$, which gives a sufficient separation between high-frequency and low-frequency wave dynamics. The lower hybrid frequency is $\omega_{LH} = \left[\omega_{pi}^{-2} + \left(\omega_{ce}\omega_{ci} \right)^{-1} \right]^{-1/2} = 1.95 \times 10^5 s^{-1}$ (31 kHz), where $\omega_{pi} = \sqrt{n_0 e^2/\epsilon_0 m_i} = 4.691 \times 10^5 s^{-1}$ (74.66 kHz) is the ion plasma frequency and $\omega_{ci} = eB_0/m_i = 4.952 \times 10^3 s^{-1}$ (0.788 kHz) is the ion cyclotron frequency. The pump amplitude E_0 is taken to be in the range 1.0 to 2.5 V/m, which are amplitudes thought to be generated by HAARP's HF heater. A summary of the physical parameters is shown in Table 1.

3. Overview of Simulation Results

We here discuss the time and space evolution of the ion density and electron temperature, as well as the various wave modes observed in a simulation using $E_0 = 2.0$ V/m. In particular, the onset of high- and low-frequency turbulence is correlated with a sharp rise in the electron temperature. While the electrons are significantly heated by the turbulence, the ions are not visibly heated, and we therefore restrict the discussion to the electron heating.

3.1. Ion Density Fluctuations

A plot of the time evolution of the ion density in space and Fourier space is shown in Figure 2. The seeded density striation shown in Figure 1 is visible in Figure 2 for $-1.5 \leq x \leq 1.5$ m. Large-amplitude ion density fluctuations appear after about 0.05 ms, in the form of a standing wave pattern oscillating in time with a frequency close to the lower hybrid frequency. The wave number spectrum of the ion density in Figure 2 shows notable features: a consistent component near $k = 10-20$ m^{-1} and another peak near $k = 40-60$ m^{-1}, corresponding to wavelengths of $\lambda = 0.30-0.60$ m and $\lambda = 0.10-0.15$ m, respectively. Wave components below $k = 3$ m^{-1} have been trimmed as they correspond to the time-stationary density striation seen in Figure 2.

Table 1. Summary of Physical Parameters Used in the Vlasov Simulations and Some Derived Plasma Parameters

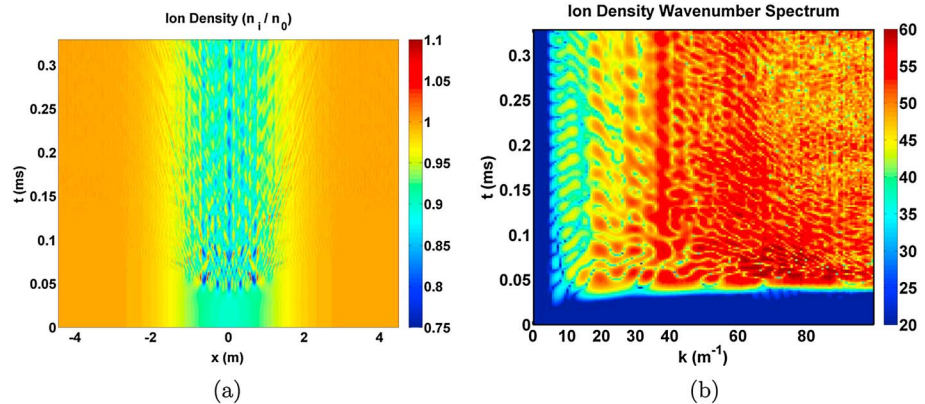| Para	Value	Para	Value	Para	Value
n_0	1.27×10^{11} m^{-3}	ω_{pe}	20.09×10^6 s^{-1} (3.197 MHz)	ω_{pi}	4.691×10^5 s^{-1} (74.66 kHz)
B_0	5.17×10^{-5} T	ω_{ce}	9.09×10^6 s^{-1} (1.447 MHz)	ω_{ci}	4.952×10^3 s^{-1} (0.788 kHz)
E_0	2.0 V/m	ω_0	21.59×10^6 s^{-1} (3.436 MHz)	ω_{LH}	1.95×10^5 s^{-1} (31 kHz)
T_{e0}	1500 K	v_{Te0}	1.508×10^5 m/s		
T_{i0}	1000 K	v_{Ti0}	2.873×10^3 m/s		

Figure 2. Time evolution of the normalized ion density n_i/n_0 in (a) space and (b) wave number space.

3.2. Electron Heating

The evolution of the electron temperature in space and time is shown in Figure 3. The electron heating is significant, with a rise of the electron temperature by several thousands of kelvin, which is correlated with the onset of lower hybrid oscillations seen in Figure 2. From Figure 3 and the snapshots of the spatial temperature profiles in Figure 4 we see that the most efficient heating occurs near the center of the striation, while the electron temperature outside the central cavity rises more slowly. The time evolution of the electron temperature, spatially averaged over the center of the striation is shown in Figure 4. After the initial 0.05 ms turn-on time, the electrons are heated rapidly to $T_e \approx 4000$ K over the next 0.05 ms, after which they heat more slowly up to $T_e \approx 6000$ K over the remaining 0.20 ms to the end of the simulation. The heating gives rise to an electron distribution function which is gyrotropic in (v_x, v_y) space. A cut of the electron distribution along v_x is shown in Figure 5. The initially Maxwellian velocity distribution widens and develops into a more flat-topped distribution as the bulk electrons are accelerated by the turbulence.

3.3. Observed High-Frequency and Low-Frequency Wave Modes

Inside of the striation, both high-frequency and low-frequency waves are excited by the external pump wave. To diagnose these, we investigate the temporal and spatial wave spectra of the simulation electric field data. We concentrate here on the frequencies covering the lower hybrid components $f < 100$ kHz and frequencies covering the upper hybrid components $3.3 < f < 3.6$ MHz. In the low-frequency spectrum in Figure 6 there is a peak between 30 and 35 kHz, near the lower hybrid frequency $f_{LH} \approx 31$ kHz (see Table 1). In the high-frequency frequency spectrum in Figure 6, the pump wave is visible at $f_0 = 3.436$ MHz, and two downshifted peaks are visible at $f = 3.41$ and 3.38 MHz. The difference in frequency between adjacent peaks in the high-frequency spectrum corresponds roughly to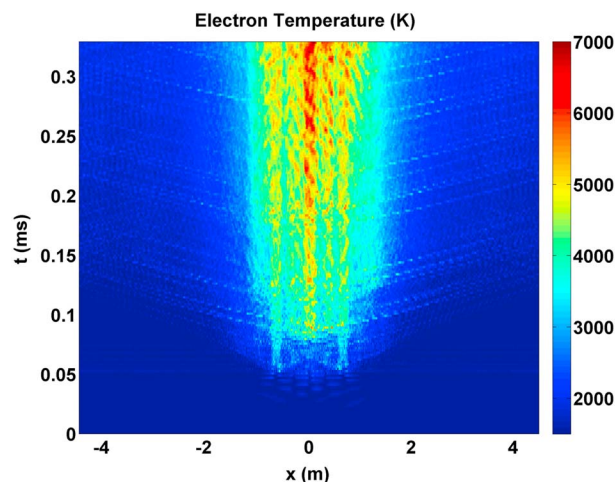 the lower hybrid frequency. After separating the frequency spectrum, the high- and low-frequency components is inverse Fourier transformed back into space and time. The amplitude of the high- and low-frequency components is shown in Figure 7. While both the high- and low-frequency waves appear to be mostly confined to the initially seeded density striation, there is noticeable leaking of high-frequency waves propagating away from the striation which we later identify as short wavelength electron Bernstein waves. Low-frequency electric fields are visible after about 0.05 ms, similar to the ion density fluctuations in Figure 1.

Plots of the wave number spectra of the low- and high-frequency components of the electric field are shown in Figure 8. For
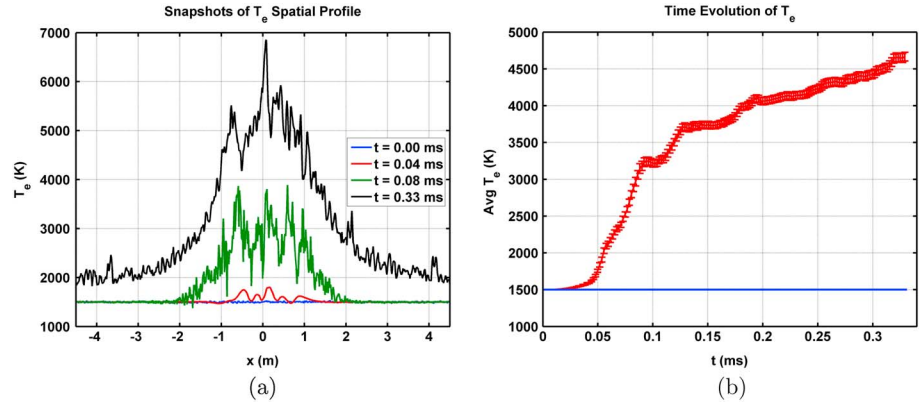

Figure 3. Evolution of the electron temperature T_e (K) in time and space.

Figure 4. (a) Spatial profiles of T_e at different times and b the time evolution of T_e averaged over space -1.5 m $\leq x \leq 1.5$ m at the center of the striation.

the most part, the components occupy distinct scales. The high-frequency components in Figure 8 show a condensation at small wave number $k < 7\,\mathrm{m}^{-1}$, while the low-frequency components in Figure 8 peak at $k \approx 7\,\mathrm{m}^{-1}$. This is typical for an inverse cascade of upper hybrid waves to smaller wave numbers, downshifted in frequency, accompanied by lower hybrid waves at larger wave numbers. There are also spectral components at large wave numbers $k \approx 50$–$70\,\mathrm{m}^{-1}$ in the low-frequency spectrum and $k \approx 40$–60 m^{-1} in the high-frequency spectrum, which we associate with short wavelength electron Bernstein waves interacting with lower hybrid waves.

The power spectrum of the electric field in wave number and frequency space is shown in Figure 9 and is compared with numerical solutions of the dispersion relations for electron Bernstein and lower hybrid waves in Figure 10. The pump wave is seen just below $f = 3.5$ MHz at $k = 0$. The immediately neighboring nonzero wave numbers are upper hybrid waves, and the spectral components extending out to higher wave numbers are associated with the second electron Bernstein mode. Similarly, the arched features near $k = 50$ m^{-1} and $f = 2.0$ MHz are associated with the first electron Bernstein mode. The electron Bernstein mode associated with the upper hybrid frequency has a resonance at the second cyclotron resonance, $f = 2f_{ce} = 2.9$ MHz, while the first electron Bernstein mode is associated with the first cyclotron resonance $f = f_{ce} = 1.45$ MHz at large wave numbers. Components of the third Bernstein mode are visible for frequencies near $f = 4.5$ MHz. Lower hybrid waves are visible for $|k| \lesssim 100$ m^{-1} and $f \lesssim 100$ kHz. The excitations of Bernstein modes at large wave numbers cover wide bands in ω-k space, which indicates that the plasma parameters change in time. The increase in the electron temperature from $T_{e0} = 1500$ to 6000 K in the striation (see Figures 3 and 4) affects the dispersion properties of the electron Bernstein modes. The dispersion relation for electron Bernstein waves is given by *Crawford and Tataronis* [1965]

$$1 + \frac{\omega_{pe}^2}{\omega_{ce}^2}\frac{\exp(-\lambda)}{\sin(\pi\Omega)} \int_0^{\pi} \sin(\psi\Omega)\sin(\psi)$$
$$\exp[-\lambda\cos(\psi)]\,\mathrm{d}\psi = 0, \quad (7)$$

where $\lambda = k^2 v_{Te}^2/\omega_{ce}^2$ and $\Omega = \omega/\omega_{ce}$. The low-frequency mode associated with lower hybrid waves is derived from the dispersion relation

$$1 + \chi_e + \chi_i = 0 \quad (8)$$

where the ion and electron susceptibilities are, respectively, given by

$$\chi_i = -\frac{\omega_{pi}^2}{\omega^2 - \omega_{ci}^2 - \gamma_i v_{Ti}^2 k^2} \quad (9)$$
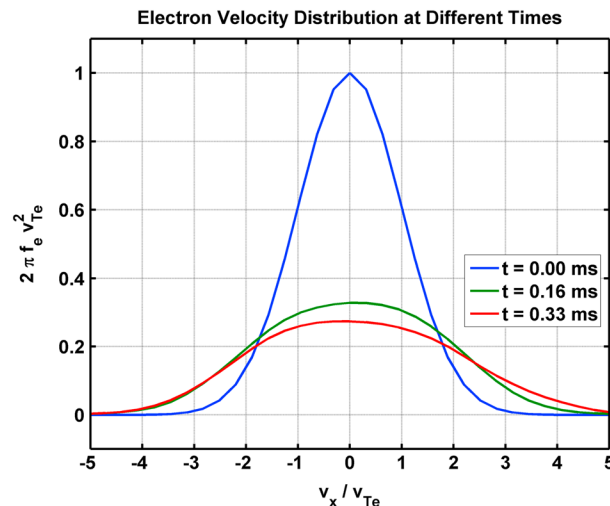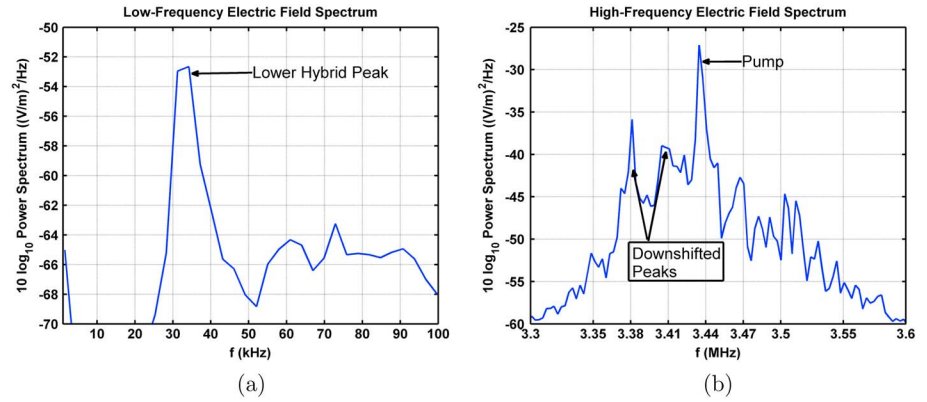

Figure 5. Profiles of the electron velocity distribution at different times. Initially, the velocity profile is Maxwellian, but as the electrons are heated, the distribution widens and becomes more flat topped.

Figure 6. Frequency spectra of the electric field showing (a) the low-frequency and (b) high-frequency components.

and

$$\chi_e = -\frac{\omega_{pe}^2}{\omega^2 - \omega_{ce}^2 - \gamma_e v_{Te}^2 k^2}. \tag{10}$$

In the frequency range $\omega_{ci}^2 \ll \omega^2 \ll \omega_{ce}^2$, we obtain the low-frequency dispersion relation

$$\omega^2 = \gamma_i v_{Ti}^2 k^2 + \frac{\omega_{pi}^2(\omega_{ce}^2 + \gamma_e v_{Te}^2 k^2)}{\omega_{pe}^2 + \omega_{ce}^2 + \gamma_e v_{Te}^2 k^2}, \tag{11}$$

where the adiabatic factors are $\gamma_i = 3$ and $\gamma_e = 1$. The electron and ion thermal effects lead to an increase of the frequency with wave number.

The three first electron Bernstein branches and the lower hybrid branch are plotted in Figure 10 for different electron temperatures. We note from Figure 10 that the electron Bernstein dispersion curves contract in wave number space for higher electron temperatures. Since the electron temperature is time-dependent in the simulations, and the Fourier transform in space and time effectively averages over time and space, Figure 9 shows signatures of electron Bernstein modes at different temperatures mapped into the same plot. By applying a Gaussian window in time and space before performing the Fourier transforms, and by shifting the center of the window in time, we obtain an approximate time dependence of the wave spectrum. A few snapshots are shown in Figure 11 with time and space centers and standard deviations, σ_x and σ_t, given for each snapshot. At $t = 0.02$ ms, we see only the pump wave and a narrow spectrum of neighboring upper hybrid waves, and a similar band of low-frequency lower hybrid waves. At $t = 0.04$ ms, electron Bernstein modes near the upper hybrid frequency are excited, but the principle components are the upper hybrid and lower hybrid waves. At $t = 0.08$ ms, the Bernstein modes have significantly increased in amplitude, and by $t = 0.30$ ms, they have clearly contracted in wave number space due to the increase of electron temperature.
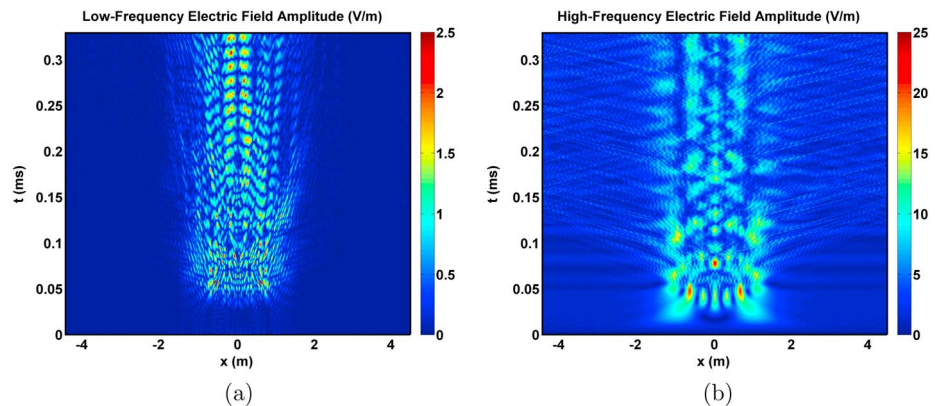

Figure 7. The amplitudes of (a) the low-frequency electric field and (b) the high-frequency electric field.
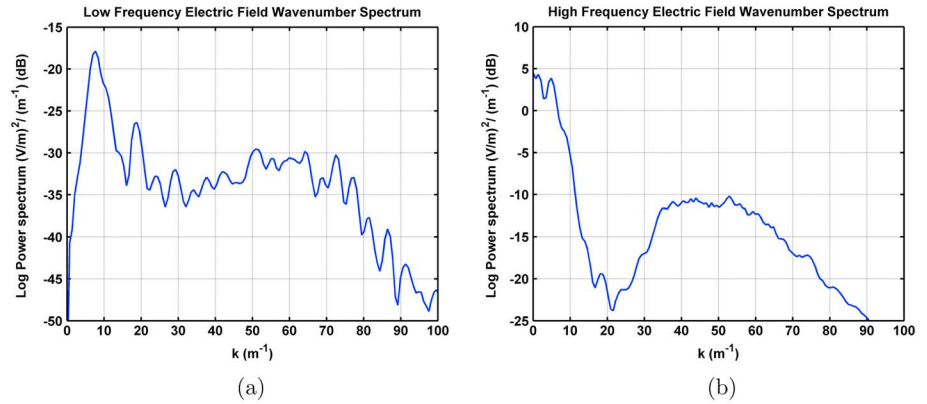
Figure 8. Electric field E_x wave number spectrum separated into (a) low-frequency and (b) high-frequency components.

4. Parametric Decay Instabilities

We here discuss parametric decay instabilities that can explain the excitations of various high- and low-frequency modes observed in the simulations.

4.1. Parametric Decay of Upper Hybrid to Upper Hybrid and Lower Hybrid Waves

Linear mode conversion of the pump wave (E_0, ω_0) to upper hybrid waves takes place at the edge of the density cavity where the plasma density is 95% of the ambient density, so that $\omega_0 = 21.59 \times 10^6$ s^{-1} (see Table 1). The mode converted upper hybrid wave can propagate to the center of the striation and interact nonlinearly with lower hybrid waves in the form of a three-wave decay creating a daughter upper hybrid wave and a lower hybrid wave. Correcting for kinetic effects of finite ω_{ce}/ω_{pe} ratio, the dispersion relation for upper hybrid waves is *Lominadze* [1981]

$$\omega^2 = \omega_{UH}^2 + \frac{3v_{Te}^2 k^2 \omega_{pe}^2}{\omega^2 - 4\omega_{ce}^2}, \tag{12}$$

which can be derived from equation (7) for $v_{Te}k/\omega_{ce} \ll 1$. The bottom of the density cavity is homogenous to first order, so we can assume a constant density at 90% of the ambient density. For a given frequency $\omega = \omega_0$, the wave number $k = k_0$ can be obtained from

$$\omega_0^2 = 0.9\omega_{pe}^2 + \omega_{ce}^2 + \frac{3v_{Te}^2 k_0^2 0.9\omega_{pe}^2}{\omega_0^2 - 4\omega_{ce}^2}.$$
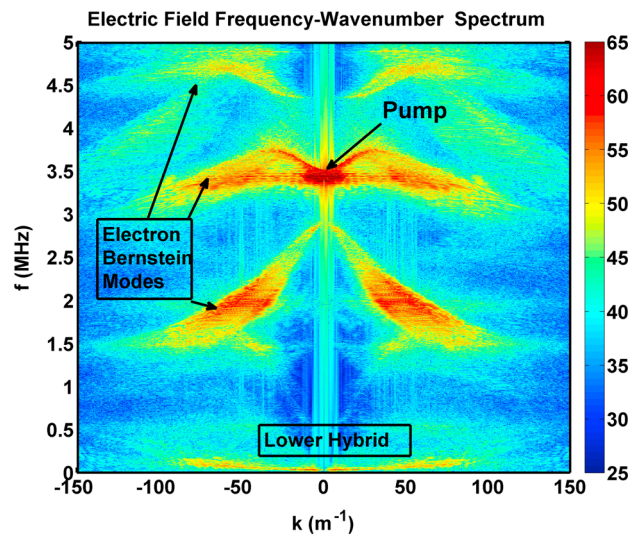

Figure 9. Frequency-wave number power spectrum of E_x ($10\log_{10}$ scale). The pump wave is seen near $k = 0$ at $f = 3.44$ MHz. Electron Bernstein modes are visible near $k = \pm 50$ m^{-1} and $f = 2.0$ MHz. Lower hybrid waves are seen for $|k| \lesssim 100$ m^{-1} and $f \lesssim 100$ kHz.

We consider three separate temperatures, the initial $T_{e0} = 1500$ K, and two temperatures $T_e = 4000$ K and $T_e = 6000$ K observed later in the simulation. For each of these temperatures and using the parameter values in Table 1, the upper hybrid wave number k_0 and associated wavelength $\lambda_0 = 2\pi/k_0$ are given in Table 2.

The lower hybrid frequency at the bottom of the striation at small wave numbers is

$$\omega_{LH} \approx \frac{1}{\sqrt{(\omega_{ci}\omega_{ce})^{-1} + \omega_{pi}^{-2}/0.9}}, \tag{13}$$

giving $\omega_{LH} = 1.92 \times 10^5$ s^{-1} (30.48 kHz). The frequency difference between the driving frequency and the local upper hybrid frequency at the bottom of the cavity is
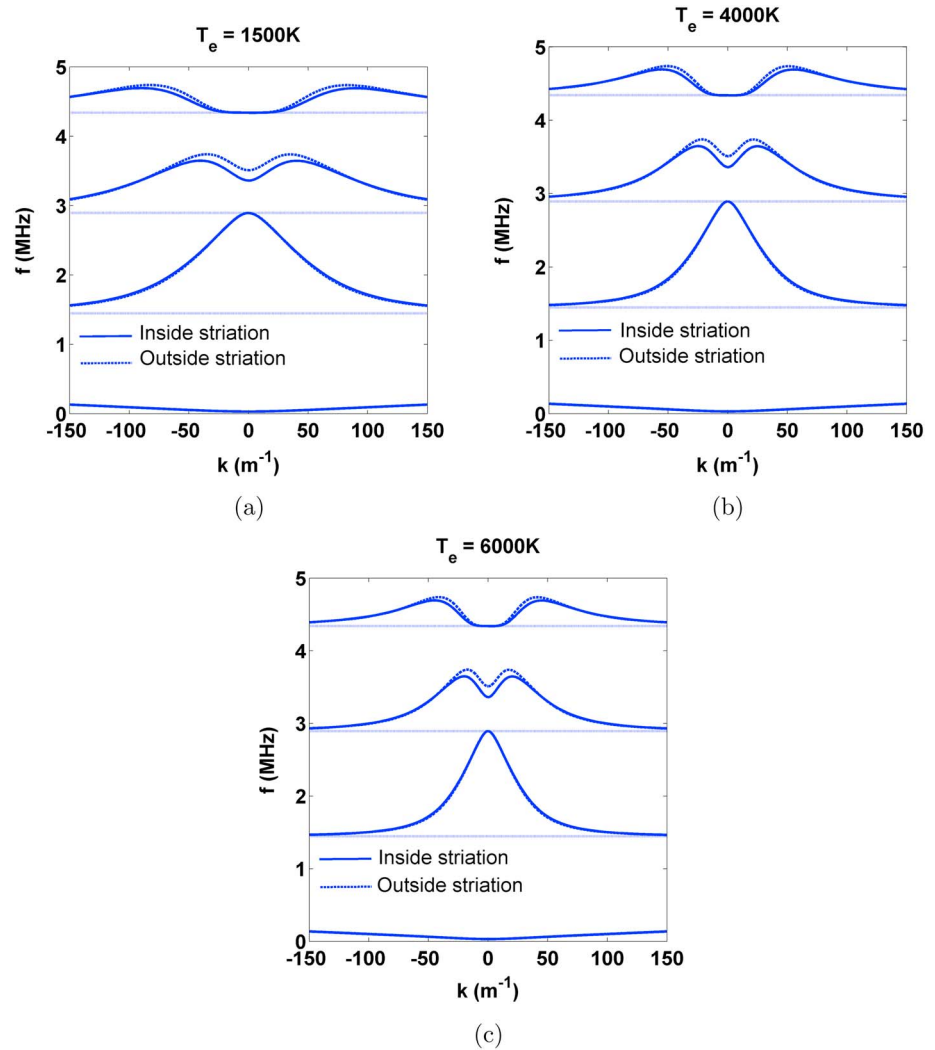
Figure 10. Electron Bernstein and lower hybrid dispersion curves for (a) 1500 K, (b) 4000 K, and (c) 6000 K. In each figure, the first three branches of the electron Bernstein modes are shown, with resonances at the respective electron cyclotron harmonic at large wave numbers.

$$\Delta\omega = \sqrt{0.95\omega_{pe}^2 + \omega_{ce}^2} - \sqrt{0.90\omega_{pe}^2 + \omega_{ce}^2},$$
$$= 4.73 \times 10^5 \text{s}^{-1} = 75.26 \text{ kHz.} \tag{14}$$

Hence, since $\Delta\omega/\omega_{LH} = 2.47$ there is sufficient room in frequency space for a double decay of upper hybrid waves to downshifted daughter upper hybrid waves, with successive downshifts equal to the lower hybrid frequency.

The three-wave decay obeys the matching conditions

$$\omega_0 = \omega_1 + \omega_{LH}, \tag{15}$$

$$k_0 = k_1 + k_{LH}. \tag{16}$$

for the frequencies and wave vectors, when an upper hybrid wave, (ω_0, k_0), decays into a daughter upper hybrid wave, (ω_1, k_1) and a lower hybrid wave, (ω_{LH}, k_{LH}). Using equation (15) to eliminate ω_1 in the upper hybrid dispersion relation for (ω_1, k_1)

$$(\omega_0 - \omega_{LH})^2 = 0.9\omega_{pe}^2 + \omega_{ce}^2 + \frac{3v_{Te}^2 k_1^2 0.9\omega_{pe}^2}{(\omega_0 - \omega_{LH})^2 - 4\omega_{ce}^2}, \tag{17}$$
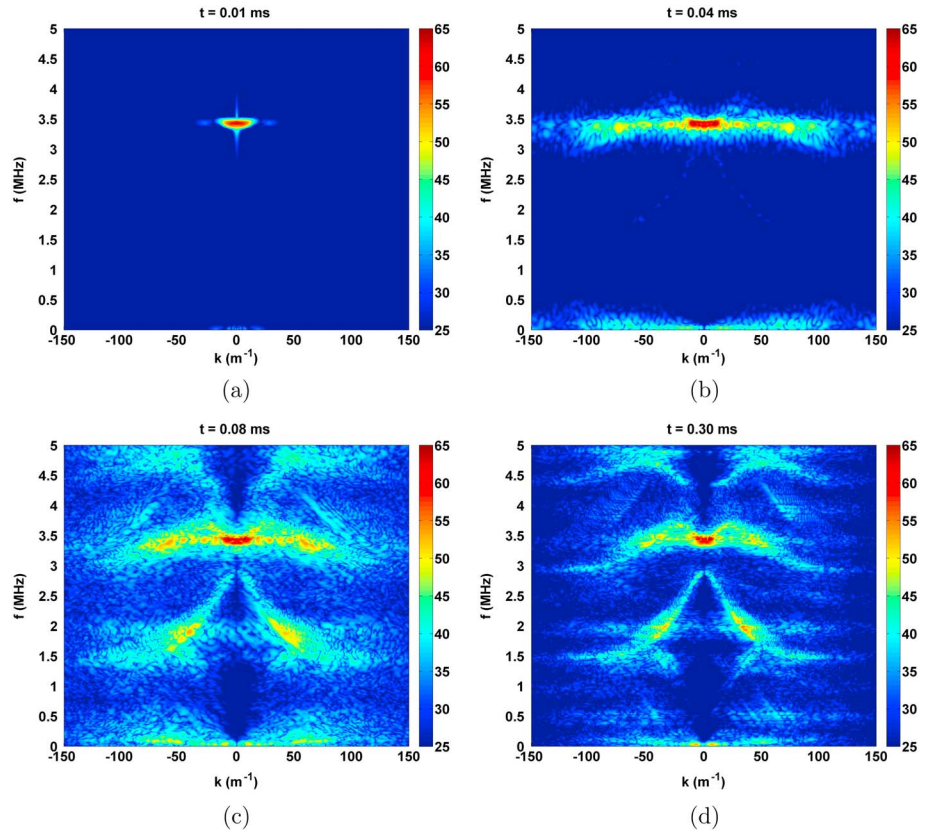
Figure 11. E_x Frequency-wave number plots with Gaussian windows to isolate the bottom of the seed density striation ($x = 0$) in space ($\sigma_x = 1\,\text{m}$) , and to cover principally $\pm 0.01\,\text{ms}$ ($\sigma_t = 0.01\,\text{ms}$) from their focus time. Shown are spectra at (a) $t = 0.02\,\text{ms}$, (b) $t = 0.04\,\text{ms}$, (c) $t = 0.05\,\text{ms}$, (d) $t = 0.30\,\text{ms}$.

from which the resulting wave numbers k_1 and wavelengths $\lambda_1 = 2\pi/k_1$ are obtained and summarized in Table 3. The corresponding lower hybrid wave number is obtained from equation (16) as $k_{\text{LH}} = k_0 - k_1$. In the second decay, the new frequency matching condition will be

$$\omega_1 = \omega_2 + \omega_{\text{LH}},$$

which combined with equation (15) gives

$$\omega_0 = \omega_2 + 2\omega_{\text{LH}}, \tag{18}$$

and the corresponding dispersion relation for (ω_2, k_2) becomes

$$\left(\omega_0 - 2\omega_{\text{LH}}\right)^2 = 0.9\omega_{\text{pe}}^2 + \omega_{\text{ce}}^2 + \frac{3v_{Te}^2 k_2^2 0.9\omega_{\text{pe}}^2}{\left(\omega_0 - 2\omega_{\text{LH}}\right)^2 - 4\omega_{\text{ce}}^2}, \tag{19}$$

Table 2. Upper Hybrid Wave Number and Wave Length for Different Electron Temperatures, Representing the Initial Temperature 1500 K and Higher Temperature 4000 K and 6000 K Observed Later in the Simulation

T_e(K)	k_0(m^{-1})	λ_0(m)
1500	10.38	0.60
4000	6.36	0.99
6000	5.19	1.21

Table 3. Daughter Upper Hybrid and Lower Hybrid Wave Number and Wavelength for Different Electron Temperatures, Representing the Initial Temperature 1500 K and Higher Temperature 4000 K and 6000 K Observed Later in the Simulation

T_e (K)	k_1 (m^{-1})	λ_1 (m)	k_{LH} (m^{-1})	λ_{LH} (m)
1500	−7.68	0.82	18.06	0.35
4000	−4.70	1.34	11.06	0.57
6000	−3.84	1.64	9.03	0.70

together with $k_{LH} = k_1 - k_2$. These results are summarized in Table 4. Thus, through a three-wave parametric decay process in two steps, the upper hybrid waves cascade to daughter upper hybrid waves at smaller wave number and downshifted by the lower hybrid frequency in each step. This corresponds to the two downshifted peaks seen near 3.41 MHz and 3.38 MHz in Figure 6. Similar results linking downshifted frequency peaks to the decay of trapped upper hybrid waves were found using fluid simulations by *Mjølhus* [1998].

In addition to the three-wave decay scenarios discussed here, it should be noted that the modulational instability (a four-wave process) and strong turbulence [*Litvak et al.*, 1983] may contribute to the localization of wave energy. Some features of localized electron heating in Figure 3 and localized high-frequency electric fields in Figure 7 during the onset of turbulence indicate that upper hybrid wave collapse takes place. In Figure 3 there are stationary pockets of heated electrons inside the striation that have the largest increase in temperatures, and in Figure 7 there are pockets of large-amplitude electric field inside the striation that collapse in advance of the onset of fast electron heating.

4.2. Parametric Decay of Upper Hybrid to Electron Bernstein and Lower Hybrid Modes

In addition to upper hybrid waves at small wave numbers, there are also excitations of electron Bernstein waves at large wave numbers, visible in Figures 9 and 11 at $k \approx 40 - 60$ m^{-1} and frequencies near 2 MHz and 3.4 MHz. These excitations are associated with the first and second electron Bernstein modes seen in Figure 10. As seen in Figure 12, an upper hybrid pump wave near 3.44 MHz can decay into frequency downshifted daughter waves on the same electron Bernstein branch at four different wave numbers, near ±50 m^{-1} and ±5 m^{-1}, and to lower hybrid waves at four different wave numbers. We see regions of the frequency-wave number spectrum consistent with this decay channel in Figure 9. Additionally, the high-wave number decay modes described here can account for the lower hybrid wave number spectrum peaks near $k = 60$ m^{-1} seen in Figure 8, which is not possible to explain by the single or double decay of an upper hybrid wave into upper hybrid and lower hybrid waves.

In Figure 12, excitations of the first electron Bernstein mode has its maximum intensity near $f = 2$ MHz and $k = 40$ m^{-1}. For the pump wave close to 3.44 MHz and with wave number $k < 10$ m^{-1}, we note that the difference between the second and the first branches of the electron Bernstein modes intersects the first branch of the electron Bernstein mode at about 1.7 MHz with $k \approx \pm50$ m^{-1}. Thus, a potential decay mode could be to two Bernstein modes of frequency 1.7 MHz but with slightly asymmetric wave numbers near $k = 50$ m^{-1} to satisfy $k_0 = k_{EB,1} + k_{EB,2}$. For a decay of the pump into one wave of 1.72 MHz and $k = 55$ m^{-1}, the frequency of the third wave should be $3.44 - 1.72 = 1.72$ MHz, while the resulting wave number is $7.01 - 55 = -47.99$ m^{-1}. These decay products are clearly seen in Figure 9 where their diffuseness is explained by the temperature dependence of the Bernstein mode dispersion curve shown in Figure 10. Notably, unlike the first decay channel, Figure 11 indicates that this mode becomes significantly excited only much later in the simulation, indicating a smaller growth rate of the instability governing the decay of an upper hybrid wave to two electron Bernstein waves.

Table 4. Double Decay Daughter Upper Hybrid and Lower Hybrid Wave Numbers and Wavelengths for Different Electron Temperatures Representing the Initial Temperature 1500 K and Higher Temperature 4000 K and 6000 K Observed Later in the Simulation

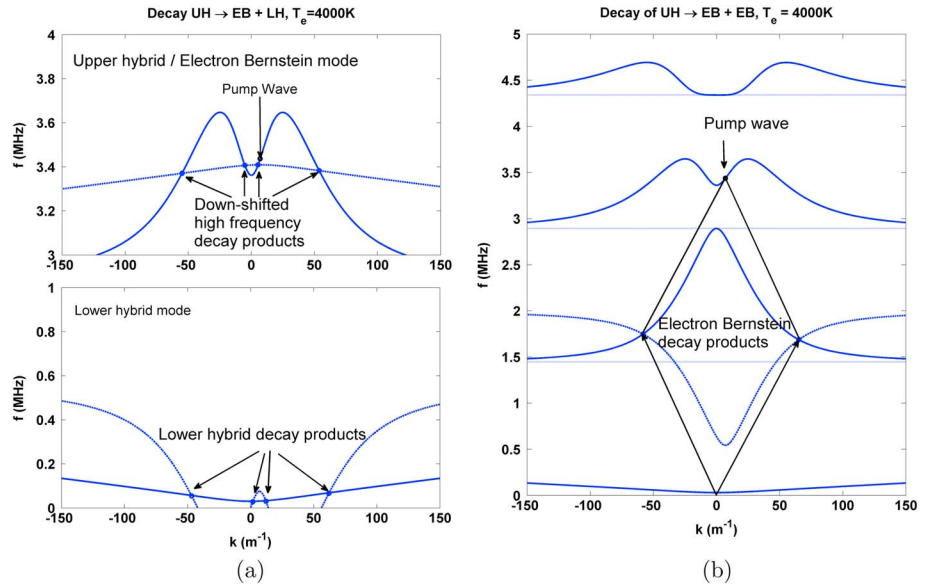| T_e (K)	k_2 (m^{-1})	λ_2 (m)	k_{LH} (m^{-1})	λ_{LH} (m)
1500	4.00	1.57	−11.69	0.54
4000	2.45	2.56	−7.16	0.88
6000	2.00	3.14	−5.84	1.08

Figure 12. Decay scenarios of a pump upper hybrid wave to (a) either a downshifted upper hybrid wave or electron Bernstein modes and a lower hybrid wave and (b) to two electron Bernstein modes.

5. Stochastic Heating Mechanism

Here we discuss the stochastic heating of electrons by large-amplitude electron Bernstein waves. It has been recognized that the acceleration of charged particles by electric field gradients perpendicular to a stationary magnetic field can lead to stochastic motion of the individual particles and a rapid heating of the plasma. The equations of motion for a charged particle in the presence of an electrostatic plane wave propagating across the ambient magnetic field can be cast into a dimensionless model problem of the form [*Karney*, 1978; *Fukuyama et al.*, 1977; *McChesney et al.*, 1987].

$$\frac{\mathrm{d}^2 v}{\mathrm{d} t^2} + v = A \cos\left(v - \Omega t\right), \tag{20}$$

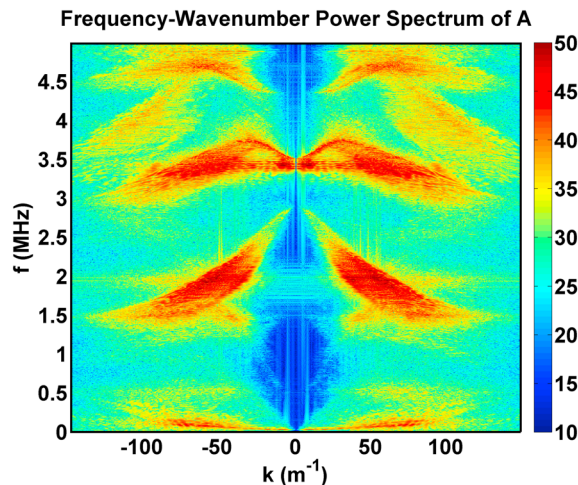$$\frac{\mathrm{d} x}{\mathrm{d} t} = v, \tag{21}$$

Figure 13. Frequency-wave number power spectrum of the normalized electric field gradient A ($10 \log_{10}$ scale). The pump wave is seen near $k = 10\ \mathrm{m}^{-1}$ and $f = 3.44$ MHz. Electron Bernstein modes near $k = \pm 50\ \mathrm{m}^{-1}$ and $f = 2.0$ MHz. Lower hybrid waves are visible for $|k| < 100\ \mathrm{m}^{-1}$ and $f \lesssim 100$ kHz.

for the particle's velocity v and position x, where $A = (mk^2\phi)/(qB_0^2)$ is a normalized wave amplitude, $\Omega = \omega/\omega_c$ is the ratio between the wave frequency and cyclotron frequency, and ϕ is the amplitude of the electrostatic potential. For small values of Ω and v, it was noted [*McChesney et al.*, 1987] that stochasticity sets in for $A \gtrsim 1$. At this value, the particle displacement due to polarization drift becomes comparable to the wavelength of the electrostatic wave, and the drift approximation breaks down. An equivalent condition for stochastic electron and ion heating by large-amplitude gradients in the electric field is [*Balikhin et al.*, 1993; *Stasiewicz et al.*, 2000]

$$|A| = \left| \frac{m}{qB_0^2} \frac{\partial E_x}{\partial x} \right| \gtrsim 1. \tag{22}$$
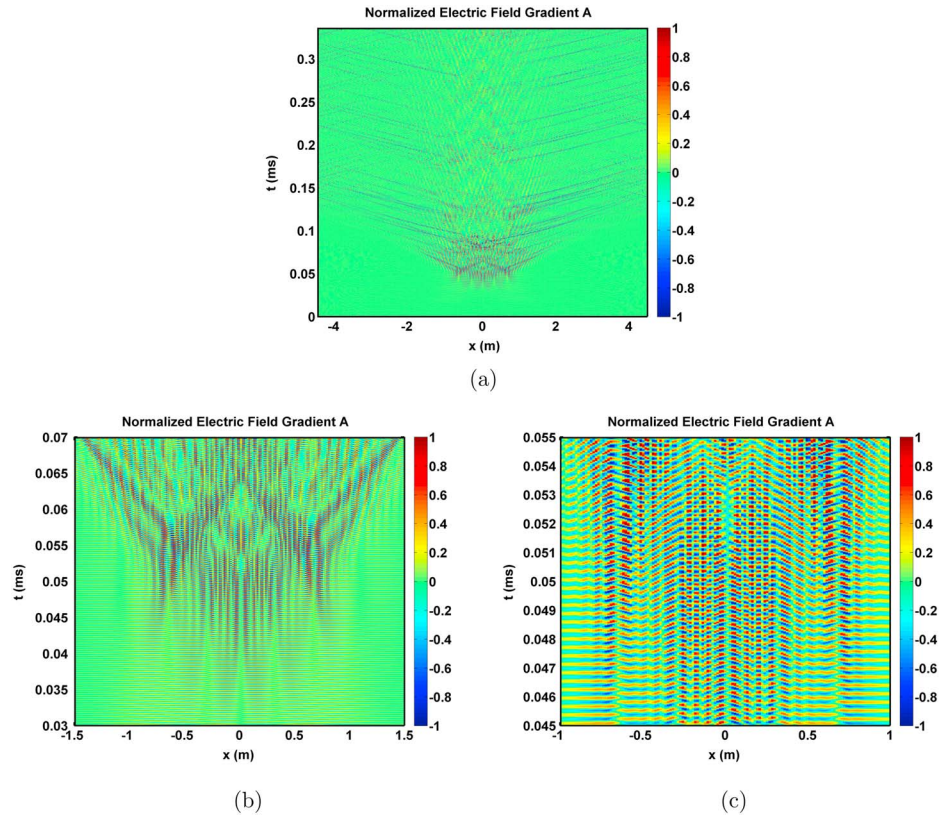
(a)

(b)

(c)

Figure 14. (a) Colormap of the normalized electric field gradient A from equation (23). (c and d) Close-ups of the initial phase of turbulence.

When this condition is fulfilled [*Balikhin et al.*, 1993] the particle orbits, initially very close in phase space, begin to diverge exponentially in time, leading to rapid heating of the particles.

5.1. Stochastic Electron Heating by Electron Bernstein Waves

Following the above ideas, we have plotted the normalized electric field gradient electric field gradient and its associated frequency wavenumber spectrum in Figures 13 and 14.

$$A = \frac{m_e}{eB_0^2} \frac{\partial E_x}{\partial x},$$
(23)

in Figure 14. Zooming in on the center of the striation near $t \approx 0.05\text{ms}$, in Figure 14 we find $|A| > 1$ which is also correlated with the characteristic turn-on time of both electron heating (Figure 4) and lower hybrid waves
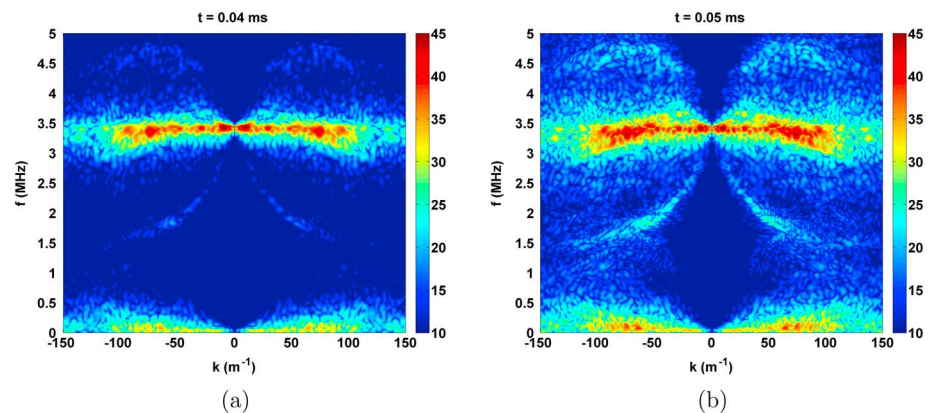

(a)

(b)

Figure 15. Windowed frequency-wave number spectra of the normalized electric field gradient A from equation (23), (a) immediately before heating burst ($t = 0.04$ ms), and (b) during heating burst ($t = 0.05$ ms).
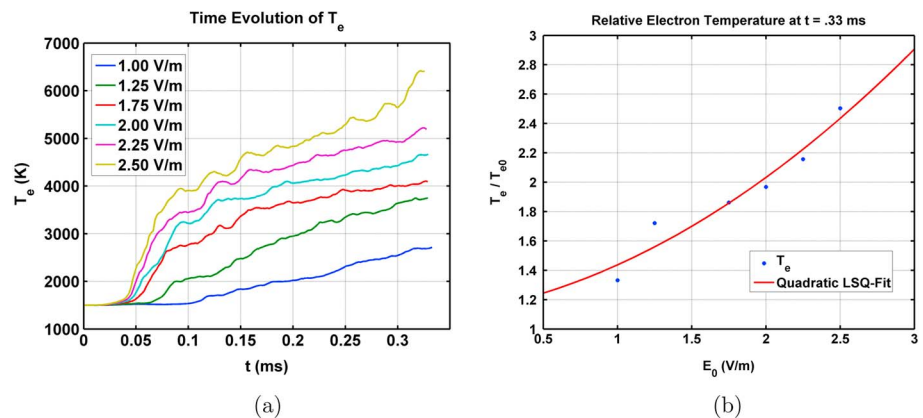
Figure 16. Scaling of the electron temperature averaged over space $-1.5\,\text{m} \leq x \leq 1.5\,\text{m}$. (a) Time dependence of T_e for different pump amplitudes and (b) the relative temperature at $t = 0.33$ ms as a function of the pump amplitudes, where the solid line shows the least squares fit to a quadratic function.

(Figure 7) in the center of the striation. High-frequency waves escaping the striation are short wavelength electron Bernstein waves, seen in Figure 14 and for $t > 0.055$ms. They contribute to the heating of the electrons outside the striation electrons at later times, seen in Figure 4.

By using windowed Fourier transforms in the same manner as in Figure 11, we can isolate which particular decay modes are associated with the stochastic heating. From Figure 15, it is evident that the primary contributions to A during the fast heating comes from frequencies near the upper hybrid frequency at a broad spectrum of large wave numbers. This indicates that the electron heating is due primarily to the decay of upper hybrid modes to short wavelength electron Bernstein waves where the large-amplitude electron Bernstein waves lead to stochastic heating of the electrons.

5.2. Scaling With Amplitude

To study the dependence of the electron heating on pump amplitude, we have carried out simulations using a series of pump amplitudes between 1.00 V/m and 2.50 V/m. We found that over the course of our simulation time, the average temperature of electrons in the density striation depends nonlinearly on the pump field. These results are summarized in Figure 16. We find that a quadratic fit for the temperature scaling with the pump field yields good agreement.

6. Summary and Conclusions

We have presented the results of Vlasov simulations of ionospheric heating near the upper hybrid resonance layer in the presence of a small-scale density striation. The pump wave mode-converts to upper hybrid waves trapped in the striation, which in turn decays to high-frequency upper hybrid and electron Bernstein waves and low-frequency lower hybrid waves. The upper hybrid and lower hybrid pairs are responsible for the inverse cascade to small wave numbers, while the electron Bernstein modes produce high-frequency, large-wave number components escaping the striation. As the amplitude of the electron Bernstein waves exceeds a threshold of stochasticity, they become the primary source of stochastic electron bulk heating. Further, we find that the average temperature inside the striations exceeds the thresholds proposed by *Eliasson et al.* [2012] for the efficient acceleration of fast electrons by strong Langmuir turbulence in the formation of descending artificial ionospheric layers. These results are relevant to active HF heating experiments performed at middle and high latitudes where injection of a pump wave near magnetic zenith results in similar geometry between the background magnetic field, field-aligned striations, and the pump wave as in these simulations. Future experiments may find evidence of these electron Bernstein waves near the first and second gyroharmonic broadband stimulated electromagnetic emission from the heated region.

References

Balikhin, M., M. Gedalin, and A. Petrukovich (1993), New mechanism for electron heating in shocks, *Phys. Rev. Lett.*, 70(9), 1259–1262, doi:10.1103/PhysRevLett.70.1259.

Blagoveshchenskaya, N. F., T. D. Borisova, T. K. Yeoman, and M. T. Rietveld (2011a), The effects of modifications of a high-latitude ionosphere by high-power HF radio waves. Part 1, *Radiophys. Q. Elec.*, 53(9–10), 512–531, doi:10.1007/s11141-011-9247-y.

Blagoveshchenskaya, N. F., et al. (2011b), The effects of modifications of a high-latitude ionosphere by high-power HF radio waves. Part 2, *Radiophys. Q. Elec.*, *54*(2), 89–101, doi:10.1007/s11141-011-9273-9.

Crawford, F. W., and J. A. Tataronis (1965), Absolute instabilities of perpendicularly propagating cyclotron harmonic plasma waves, *J. Appl. Phys.*, *36*, 2930–2934, doi:10.1063/1.1714609.

Dysthe, K. B., E. Mjølhus, H. L. Pecseli, and K. Rypdal (1982), Thermal cavitons, *Phys. Scr.*, *T2B*, 548–559, doi:10.1088/0031-8949/1982/T2B/040.

Eliasson, B. (2010), Numerical simulations of the fourier transformed Vlasov-Maxwell system in higher dimensions—Theory and applications, *Trans. Theor. Stat. Phys.*, *39*(5), 387–465, doi:10.1080/00411450.2011.563711.

Eliasson, B., X. Shao, G. Milikh, E. V. Mishin, and K. Papadopoulos (2012), Numerical modeling of artificial ionospheric layers driven by high-power HF heating, *J. Geophys. Res.*, *117*, A10321, doi:10.1029/2012JA018105.

Fukuyama, A., H. Momota, and R. Itatani (1977), Stochastic acceleration by an electrostatic wave near ion cyclotron harmonics, *Phys. Rev. Lett.*, *38*(13), 701–704, doi:10.1103/PhysRevLett.38.701.

Gurevich, A. V. (2007), Nonlinear effects in the ionosphere, *Physics-Uspekhi*, *50*(11), 1091–1121, doi:10.1070/PU2007v050n11ABEH006212.

Gurevich, A. V., K. P. Zybin, and A. V. Lukyanov (1995), Stationary striations developed in the ionospheric modification, *Phys. Rev. Lett.*, *75*, 2622–2625, doi:10.1103/PhysRevLett.75.2622.

Karney, C. F. F. (1978), Stochastic ion heating by a lower hybrid wave, *Phys. Fluids*, *21*, 1584–1599, doi:10.1063/1.862406.

Franz, T. L., M. C. Kelley, and A. V. Gurevich (1999), Radar backscattering from artificial field-aligned irregularities, *Radio Sci.*, *34*(2), 465–475, doi:10.1029/1998RS900035.

Lominadze, D. G. (1981), *Cyclotron Waves in Plasmas*, Oxford Pergamon Press.

Litvak, A. G., V. I. Petrukhina, A. M. Sergeev, and G. M. Zhislin (1983), Dynamics of one-dimensional upper-hybrid turbulence in a magnetized plasma, *Phys. Lett. A*, *94*(2), 85–88, doi:10.1016/0375-9601(83)90213-X.

McChesney, J. M., R. A. Stern, and P. M. Bellan (1987), Observations of fast stochastic ion heating by drift waves, *Phys. Rev. Lett.*, *59*(13), 1436–1439, doi:10.1103/PhysRevLett.59.1436.

Mishin, E., and T. Pedersen (2011), Ionizing wave via high-power HF acceleration, *Geophys. Res. Lett.*, *38*, L01105, doi:10.1029/2010GL046045.

Mjølhus, E. (1998), Theoretical model for long time stimulated electromagnetic emission generation in ionospheric radio modification experiments, *J. Geophys. Res.*, *103*(A7), 14,711–14,729, doi:10.1029/98JA00927.

Pedersen, T., B. Gustavsson, E. Mishin, E. MacKenzie, H. C. Carlson, M. Starks, and T. Mills (2009), Optical ring formation and ionization production in high-power HF heating experiments at HAARP, *Geophys. Res. Lett.*, *36*, L18107, doi:10.1029/2009GL040047.

Rao, P. B., and G. D. Thome (1974), A model for RF scattering from field-aligned heater-induced irregularities, *Radio Sci.*, *9*, 987–996, doi:10.1029/RS009i011p00987.

Stasiewicz, K., R. Lundin, and G. Marklund (2000), Stochastic ion heating by orbit chaotization on electrostatic waves and nonlinear structures, *Phys. Scr.*, *84*, 60–63, doi:10.1238/Physica.Topical.084a00060.